

Hole spin splitting in a Ge quantum dot with finite barriers

Jiawei Wang, Xuedong Hu, Herbert F Fotso

Department of Physics, University at Buffalo, The State University of New York, Buffalo, NY 14260-1500

(Dated: March 17, 2025)

We study the low-energy spectrum of a single hole confined in a planar Ge quantum dot (QD) within the effective-mass formalism. The QD is sandwiched between two GeSi barriers of finite potential height grown along the [001] direction. To treat this finite barrier problem, we adopt an independent-band approach in dealing with boundary conditions. The effects of different system parameters are investigated, including the width of the out-of-plane confining well, the size of the dot, and silicon concentration in the confining layers. The more accurate finite-barrier model results in the non-negligible dependence of the anisotropic g -factor on the choice of boundary conditions and on the silicon concentration in the barrier. Furthermore, while the ideal model of a planar dot with a square-well heterostructure already has an intrinsic spin-orbit coupling, realistic effects arising from the experimental setup may give rise to additional contributions. We investigate the impact from the top-gate electric field and the residual tensile strain on the qubit states. The results indicate that these effects are important contributions to the total spin-orbit coupling which enables fast electric control.

I. INTRODUCTION

Spin qubits in semiconductors, especially those based on electron spin, have attracted sustained attention due to their promise for scalability, backed by the sophisticated semiconductor fabrication technologies [1–9]. Group IV semiconductors, such as Si and Ge, are preferred host materials due to the abundance of zero-spin isotopes and possible isotopic enrichment, which suppresses nuclear spin-induced decoherence. The electron spins in these systems are also controllable both magnetically, via traditional electron spin resonance, and electrically, via electric dipole spin resonance (EDSR) [10]. While conduction electron spins in Si quantum dots (QD) have been shown to be promising [11–16],

one potentially significant challenge in the long term is the need for micromagnets in order to enable fast EDSR because of the relatively weak spin-orbit coupling. This adds to the complexities of device fabrication and multi-qubit control. As an alternative, hole spins have recently emerged as a viable qubit candidate due to the potential for intrinsically fast electrical control and the added benefit that the underlying atomic p orbital helps eliminate the contact hyperfine interaction with nuclear spins [17–33]. There has also been experimental evidence that hole spin qubits could have a relatively long coherence time, especially compared to their fast operations [34–36]. Recent experiments have already demonstrated multi-qubit processors and strong coupling to a superconducting resonator based on hole spins [37–40].

The effective spin-orbit coupling of holes that enables fast electrical control mostly originates from the strong mixing of valence bands at finite momentum. This mixing has strong k dependence and thus is sensitive to system dimensions including the thickness of the heterostructure and the strength of the electrical confinement of the quantum dot. It can also enhance the mixing of quantum dot orbitals and lead to spin splitting beyond the linear regime. Therefore, a comprehensive study of

hole spin properties must account for its dependence on system geometry and dimension, as well as the applied electric and magnetic fields.

Theoretical studies of hole spin qubits are usually based on the $\mathbf{k} \cdot \mathbf{p}$ method, as the states of the confined holes are typically dominated by contributions from near the first Brillouin zone center [34, 41–47]. In planar germanium structures, the four-band Luttinger-Kohn model is considered adequate because the most important multi-band effect is the coupling between heavy holes (HH) and light holes (LH) [48]. The more recently developed Burt-Foreman model [49–53] can further improve the accuracy of the theoretical prediction, as it avoids the use of artificial symmetrization in heterostructures [54]. Spectral properties of a hole in a QD can then be calculated by expanding the Hamiltonian over single-band single-hole orbitals (the so-called Linear Combination of Atomic Orbitals, or LCAO, approach).

A convenient assumption in choosing the orthonormal basis orbitals for the LCAO calculation is that the Ge quantum well is sandwiched between infinite barriers. This approximation simplifies the calculations by considering material properties of the confined layer only, neglects the fact that the number of quantized orbitals inside the well is finite, and most conveniently, has the wave function vanish at the two boundaries of the quantum well. In reality, however, in a $\text{Ge}_{1-\alpha}\text{Si}_\alpha\text{-Ge-Ge}_{1-\alpha}\text{Si}_\alpha$ heterostructure, with a typical 20% Si in the barrier, the barrier height is only about 132meV. Considering that the typical heavy-hole-light-hole (HH-LH) splitting (Δ_{HL}) in a Ge quantum well is several tens of meV, and the confinement energy for light holes along the growth direction is also in that order, the barriers are far from infinite. If a strong electric field is applied along the growth direction, a confined hole tunneling out of the QD becomes a realistic possibility if the potential barrier is finite, while it is not possible in the case of an infinite barrier no matter how large the electric field is. With finite barriers, the abrupt change of Luttinger/Foreman parameters at the

well-barrier interfaces can couple boundary conditions of different bands [55–57], and spurious solutions are known to appear when solving for the eigenenergies [58]. In short, to lay a solid foundation for our understanding of hole spin qubits, a systematic treatment of a Ge QD that adopts realistic parameters and conditions, and accounts for the boundary conditions properly, is still needed.

Here we present a theoretical analysis of the spectra of a single hole in a planar quantum dot based on a $\text{Ge}_{1-\alpha}\text{Si}_\alpha\text{-Ge-Ge}_{1-\alpha}\text{Si}_\alpha$ heterostructure. We modeled the heterostructure using a finite square well combined with an in-plane harmonic potential. Calculations are done using the LCAO technique with single-band QD orbitals. Our focus is on the spin splitting of the lowest heavy-hole states, which form the hole spin qubit. A uniform magnetic field is applied in the in-plane or out-of-plane directions. We study the dependence of the qubit spin splitting on silicon concentration in the barrier material at different dot sizes, as well as quantum well widths and magnetic field directions. We also evaluate the impacts of different treatments of the boundary conditions. Furthermore, we quantitatively study how the top-gate electric field and the residual strain in the barriers affect the spin splitting. Our analysis presented in this paper represents a reliable starting point for further theoretical studies of hole spin properties.

II. MODEL AND METHOD

A. System Hamiltonian

The Ge planar quantum dot is shown schematically in Fig. 1. Along the growth direction, the strained germanium layer is sandwiched between two silicon-germanium alloys, thus forming a quantum well for holes in the valence band. The top metal gates provide the in-plane confinement for the holes. The total confinement potential is thus separated into the in-plane part and the out-of-plane part. The total Hamiltonian of our system in a magnetic field is given by

$$H = H_{\text{BF}} \left(\mathbf{k} + \frac{e\mathbf{A}}{\hbar} \right) + V_\perp(z) + V_\parallel(x, y) + H_{\text{strain}} + H_{\text{Zeeman}}. \quad (1)$$

The gauge used in this study is the symmetric gauge

$$\mathbf{A} = \frac{1}{2}(B_y z - B_z y)\mathbf{e}_x + \frac{1}{2}(B_z x - B_x z)\mathbf{e}_y + \frac{1}{2}(B_x y - B_y x)\mathbf{e}_z. \quad (2)$$

Confinement in the growth direction determines the quantization axis for the holes. Therefore, the four-band Burt-Foreman Hamiltonian in the $|j, j_z\rangle$ basis with $j = 3/2$ takes the form

$$H_{\text{BF}}(\mathbf{k}) = \begin{pmatrix} P+Q & S_- & R & 0 \\ S_-^\dagger & P-Q & C & R \\ R^\dagger & C^\dagger & P-Q & -S_+ \\ 0 & R^\dagger & -S_+^\dagger & P+Q \end{pmatrix}. \quad (3)$$

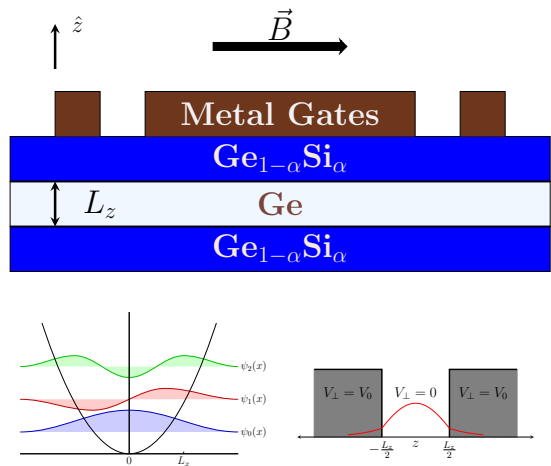


FIG. 1. Schematic figure of a planar Ge quantum dot in an in-plane magnetic field: (upper) Illustration of the heterostructure; (lower left) The in-plane confinement with harmonic potential; (lower right) The out-of-plane confinement is modeled with a finite square well.

Conventionally, heavy holes (HH) refer to the two $j_z = |3/2\rangle$ states, while light holes (LH) refer to the two $j_z = |1/2\rangle$ states. The matrix elements are defined by:

$$\begin{aligned} P &= \frac{\hbar^2 \gamma_1}{2m_0} (k_x^2 + k_y^2 + k_z^2), \\ Q &= \frac{\hbar^2 \gamma_2}{2m_0} (k_x^2 + k_y^2 - 2k_z^2), \\ R &= -\frac{\sqrt{3}\hbar^2}{2m_0} (\bar{\gamma}k_-^2 - \mu k_+^2), \\ S_\pm &= -\frac{\sqrt{3}\hbar^2}{m_0} [k_\pm(\sigma - \delta)k_z + k_z \pi k_\pm], \\ C &= -\frac{\hbar^2}{m_0} [k_-(\sigma - \delta - \pi)k_z - k_z(\sigma - \delta - \pi)k_-], \end{aligned} \quad (4)$$

where $k_\pm = k_x \pm ik_y$, and $\bar{\gamma}$, μ , σ , π , δ are Foreman parameters obtained from linear combinations of Luttinger parameters γ_1 , γ_2 , γ_3 , as shown in Appendix B. Matrix element C , which does not appear in the Luttinger-Kohn Hamiltonian, is the LH-LH coupling originating from the exact envelope-function treatment. It does not affect the bulk dispersion of a material, but may have a non-negligible contribution if boundary conditions introduce coupling between different bands [53]. Nevertheless, this LH-LH coupling may be negligible in a realistic strained heterostructure. There is a sign difference between (3) here and the original Foreman representation. It arises from the choice of different zone center states as shown in Appendix A.

In our system, the germanium layer is sandwiched between two layers of relaxed silicon-germanium alloy in the out-of-plane direction. The germanium lattice is thus uniaxially strained, compressed in the in-plane directions by the relaxed $\text{Ge}_{1-\alpha}\text{Si}_\alpha$ due to the lattice-

matched growth process, and stretched in the growth direction. Consequently, there are finite strain contributions to the diagonal matrix elements of H_{BF} via the Bir-Pikus Hamiltonian [59, 60]

$$\begin{aligned} P_\varepsilon &= -a_v(\varepsilon_{xx} + \varepsilon_{yy} + \varepsilon_{zz}), \\ Q_\varepsilon &= -\frac{b_v}{2}(\varepsilon_{xx} + \varepsilon_{yy} - 2\varepsilon_{zz}). \end{aligned} \quad (5)$$

Here, a_v is the hydrostatic deformation potential, b_v is the uniaxial deformation potential, and ε_{ij} are components of the strain tensor. The strain profile in such a Ge quantum well increases the splitting between the HH and LH bands at the Γ point.

In the envelope-function approximation, the out-of-plane confinement is provided by the valence-band offset between the strained Ge layer and the relaxed GeSi alloy, together with the uniaxial strain contribution, and is modeled by a one-dimensional finite square well. The band offset contribution takes the form

$$V_\perp(z) = \begin{cases} 0, & |z| \leq \frac{L_z}{2}, \\ V_0, & |z| > \frac{L_z}{2}, \end{cases} \quad (6)$$

where L_z is the well width. The barrier height V_0 is given in Appendix B. Such a band offset, combined with the

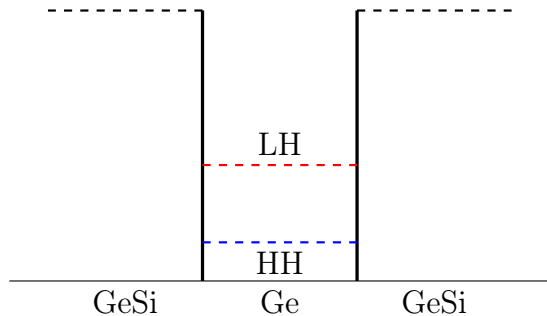


FIG. 2. Band alignment of the Ge/GeSi heterostructure with a combination of the valence-band offset and the uniaxial strain by the lattice matching mechanism.

uniaxial strain, will give an effective barrier height

$$V_{\text{eff}}(z) = V_\perp(z) + H_{\text{strain}}. \quad (7)$$

Notice that the barrier height is different for HH and LH bands, as shown in Fig. 2.

The in-plane confinement is modeled as a two-dimensional harmonic potential,

$$V_\parallel(x, y) = \frac{1}{2}m_\parallel(\omega_x^2 x^2 + \omega_y^2 y^2). \quad (8)$$

Here m_\parallel refers to the in-plane effective mass of $j_z = |3/2|$ states $m_\parallel = m_0/(\gamma_1 + \gamma_2)$. The in-plane confinement is often described in terms of effective dot sizes L_x and L_y , where $L_{x,y} = \sqrt{\hbar/(m_\parallel\omega_{x,y})}$. In this work, we focus on the case of circular confinement $L_x = L_y$.

Since the in-plane confinement is defined by the electrostatic potential produced by the top gates, it is the same for HH and LH states. Consequently, the effective dot sizes are different for HH and LH states because of their different in-plane masses. The different length scales mean that HH and LH orbitals are generally not orthogonal to each other, complicating the calculation of HH-LH coupling matrix elements, as shown in Appendix C.

Lastly, the Zeeman Hamiltonian for $j = 3/2$ states is

$$H_{\text{Zeeman}} = 2\kappa\mu_B\mathbf{B} \cdot \mathbf{J} + 2q\mu_B\mathbf{B} \cdot \mathcal{J}, \quad (9)$$

where $\mathbf{J} = (J_x, J_y, J_z)$ and $\mathcal{J} = (J_x^3, J_y^3, J_z^3)$, μ_B is the Bohr magneton ($\approx 57.88 \mu\text{eV} \cdot \text{T}^{-1}$), while the isotropic and anisotropic g -factors κ and q are material-dependent.

B. Boundary conditions

One of the most challenging aspects of studying hole properties in a finite-barrier quantum well is to determine the appropriate boundary conditions. In the envelope-function approximation, the total wave function takes the form

$$\Psi(x, y, z) = \sum_l \psi_l(x, y) \phi_l(z) u_{l0}(\mathbf{r}), \quad (10)$$

where $\psi_l(x, y)$ and $\phi_l(z)$ are the in-plane and out-of-plane components of the envelope function in band l , and u_{l0} is the corresponding Bloch function at the zone center. In general, the total wave function and its first derivative in the growth direction should be continuous at the boundaries of a finite well,

$$\Psi(x, y, z_{0+}) = \Psi(x, y, z_{0-}), \quad (11)$$

$$\partial_z \Psi(x, y, z)|_{z_{0+}} = \partial_z \Psi(x, y, z)|_{z_{0-}}, \quad (12)$$

where z_0 refers to either of the edges of the quantum well $z_0 = \pm L_z/2$. The second boundary condition is usually in the form of continuity of probability current in the z direction

$$j(z) = \int \int \Psi^* \partial_z \Psi dx dy. \quad (13)$$

Heterostructures, such as the Ge/SiGe system we study here, are built from layers of materials with similar properties. Therefore, the $\mathbf{k} \cdot \mathbf{p}$ formalism assumes that the Γ -point Bloch functions remain the same in different layers. Such an assumption leads to the continuity of the envelope functions in each band

$$\phi^{(w)}(z_0) = \phi^{(b)}(z_0). \quad (14)$$

On the other hand, in the $\mathbf{k} \cdot \mathbf{p}$ formalism, the second boundary condition is subtle due to considerations regarding the effective mass in different materials. Below, we consider two scenarios.

1. One-band model

Conduction electrons in semiconductors with weak spin-orbit coupling are usually described with a one-band model. In the case of holes in a quantum dot, the one-band model is also the usual choice for basis states in the LCAO calculations. The second boundary condition within the one-band model is the BenDaniel-Duke type [61]

$$\frac{1}{m_w} \frac{\partial \phi_w}{\partial z} \Big|_{z_{0+}} = \frac{1}{m_b} \frac{\partial \phi_b}{\partial z} \Big|_{z_{0-}}. \quad (15)$$

For a finite square well, the z component of the envelope function is a sinusoidal wave (with wave vector k_z) in the well and an evanescent wave (with inverse decay length scale χ_z) in the barrier. The Schrödinger equation in different layers then leads to the relationship

$$\frac{\hbar^2 k_z^2}{2m_w} = -\frac{\hbar^2 \chi_z^2}{2m_b} + V_{\text{eff}}(z). \quad (16)$$

Combining all the equations, we can solve the problem similar to the textbook finite square well problem.

In general, material properties are different across the layers in a heterostructure, which means all Luttinger-/Foreman parameters as well as material g -factors in the Zeeman term should be layer-dependent. In order to be consistent with the abrupt-barrier model (6), material parameters should be step functions at each boundary. This sudden change should be relatively small considering that layers in a heterostructure have similar compositions and are lattice-matched. Therefore, the lowest-order approximation here is to neglect the small changes and take these parameters as a constant across the boundaries [17, 47], which is also consistent with the

assumption that the zone center Bloch states are the same across the boundaries.

Alternatively, if one ignores the same-Bloch-state assumption and emphasizes the fact that materials in different layers are different (here it is Ge vs $\text{Ge}_{1-\alpha}\text{Si}_\alpha$), it also seems reasonable to assume a change of effective mass along the growth direction.

2. Multi-band model: the coupled boundary conditions

One-band model treats the boundary conditions at the lowest-order approximation, though such an independent-band assumption is questionable. Instead, the four-band Burt-Foreman Hamiltonian is the minimal model for holes in a quantum dot due to the strong HH-LH coupling away from the Brillouin zone center. The boundary conditions for a confined hole are thus in general in the matrix form. Specifically, assuming that Luttinger/Foreman parameters undergo sudden changes at a boundary, the strong HH-LH coupling in H_{BF} would then lead to coupled boundary conditions in the four-band description of the holes. In other words, the continuity of probability current becomes a matrix equation

$$\mathcal{D}^{(w)} |\phi^{(w)}\rangle = \mathcal{D}^{(b)} |\phi^{(b)}\rangle, \quad (17)$$

where the solution

$$|\phi\rangle = \left(\phi^{3/2}(z) \quad \phi^{1/2}(z) \quad \phi^{-1/2}(z) \quad \phi^{-3/2}(z) \right)^T, \quad (18)$$

contains envelope functions from all four bands. The derivative operator in the Luttinger-Kohn model or in the Burt-Foreman model is [53, 58]

$$\begin{aligned} \mathcal{D}_{\text{LK}} &= \begin{pmatrix} (\gamma_1 - 2\gamma_2) \frac{\partial}{\partial z} & -\sqrt{3}i\gamma_3 k_- & 0 & 0 \\ \sqrt{3}i\gamma_3 k_+ & (\gamma_1 + 2\gamma_2) \frac{\partial}{\partial z} & 0 & 0 \\ 0 & 0 & (\gamma_1 + 2\gamma_2) \frac{\partial}{\partial z} & \sqrt{3}i\gamma_3 k_- \\ 0 & 0 & -\sqrt{3}i\gamma_3 k_+ & (\gamma_1 - 2\gamma_2) \frac{\partial}{\partial z} \end{pmatrix} \\ \mathcal{D}_{\text{BF}} &= \begin{pmatrix} (\gamma_1 - 2\gamma_2) \frac{\partial}{\partial z} & -2\sqrt{3}i\pi k_- & 0 & 0 \\ 2\sqrt{3}i(\sigma - \delta)k_+ & (\gamma_1 + 2\gamma_2) \frac{\partial}{\partial z} & 2i(\sigma - \delta - \pi)k_- & 0 \\ 0 & -2i(\sigma - \delta - \pi)k_+ & (\gamma_1 + 2\gamma_2) \frac{\partial}{\partial z} & 2\sqrt{3}i\pi k_- \\ 0 & 0 & -2\sqrt{3}i(\sigma - \delta)k_+ & (\gamma_1 - 2\gamma_2) \frac{\partial}{\partial z} \end{pmatrix} \end{aligned} \quad (19)$$

where the Luttinger parameters γ_1 , γ_2 , and γ_3 are different across the boundary

$$\gamma_i(z) = \begin{cases} \gamma_i^{(w)}, & |z| \leq \frac{L_z}{2} \\ \gamma_i^{(b)}, & |z| > \frac{L_z}{2} \end{cases}, \quad (20)$$

The Foreman parameters σ , δ , π are similarly defined.

Solving such an eigenvalue problem becomes highly

non-trivial. Early studies include calculations of band structures in superlattices [56, 62] and quantum wells [57, 58, 63–66]. However, the eigenvalue techniques adopted in these studies are not straightforwardly applicable in the current work: in quantum dots the in-plane wave vectors k_\pm become operators. In this case, one has to solve a large set of coupled differential equations, and many spurious solutions may appear even if the problem

is solvable [58].

In appendix D, we propose a possible treatment to modify the single-band basis states of the quantum well in an effort to construct a total envelope function that satisfies the coupled boundary conditions. Interestingly, we find that the coupled boundary conditions do not modify the single-band basis states significantly from the uncoupled ones. As such, our current LCAO calculations are still constructed upon the basis states from a one-band model.

C. Numerical Method

The four-band problem for a single hole confined in a quantum dot can only be solved numerically. We first solve the in-plane and the out-of-plane effective mass states individually in the corresponding confining potentials, obtaining the single-band basis states as products of the two. We then construct the matrix representation of the total Hamiltonian over these single-band orbitals, and diagonalize the Hamiltonian to obtain its energy spectrum.

The out-of-plane states are solutions of the finite square well. Calculations are done self-consistently by considering all the bound states in the quantum well. Therefore, the number of quantum-well sub-bands depends on the system setup. For example, for a typical silicon concentration of $\alpha = 0.2$, the effective barrier heights are 142meV for HH and 81meV for LH. In this situation, a 14-nm-wide quantum well has 5 bound states for each HH band and 2 bound states for each LH band.

The in-plane states are solutions of a 2D harmonic oscillator if an in-plane \mathbf{B} field is applied, or Fock-Darwin states if the field is along the z direction. The number of in-plane orbitals is 15 for each band in our calculations. This number of orbitals can already provide satisfactory convergence; adding more orbitals will not significantly change the result.

III. SPECTRAL STUDIES OF A HOLE SPIN

In this section, we discuss our numerical analysis of the spin spectra of the ground heavy-hole state in a single-hole Ge planar quantum dot. Our main objective is to obtain hole spectral properties with a realistic treatment of the quantum dot confinement, particularly along the growth direction. By exploring such an effective finite well, we can relate hole properties to material properties and experimental conditions such as the content of Si in the GeSi barrier (which directly relates to the height of the finite barrier), the degree of strain in the Ge well, the width of the quantum well, and the applied electric and magnetic fields.

As we discussed in the previous section, there are certain ambiguities with respect to the finite well boundary condition, such as whether we should assume that the

effective mass changes across the boundary or not. Consequently, we perform our calculations under both conditions. Results obtained with a sudden change of effective masses are labeled as “shifted- m^* ”, while results obtained neglecting this sudden change are labeled as “fixed- m^* ”. The ultimate judge on these two approaches can only be given experimentally.

In all the calculations, material properties in the $\text{Ge}_{1-\alpha}\text{Si}_\alpha$ alloy are based on linear interpolation of parameters in Si and Ge. In general, the larger α is (the larger concentration of Si), the higher the barrier. On the other hand, larger α also means larger lattice mismatch between the alloy (which is relaxed) and the Ge quantum well. To have a sufficiently high barrier to confine the holes, while also allowing high-quality lattice-matched growth of strained Ge quantum well, we limit our calculations to a range of α from 0.15 to 0.25. This provides a reasonable barrier height, and the alloy is germanium-like. All the other relevant parameters used in this paper can be found in Appendix B.

A. Energy spectra in an applied \mathbf{B}_{\parallel} field

We first calculate the energy spectra of the planar quantum dot in a \mathbf{B}_{\parallel} field. The lowest two spin states are shown in Fig. 3. The inset of Fig. 3 is the qubit Zeeman splitting of these lowest two levels as a function of the magnetic field strength. The purple dots are the numerical output, while the blue dashed line shows the corresponding linear trend in the weak-field limit. The spin splitting maintains a good linearity up to at least 0.75T.

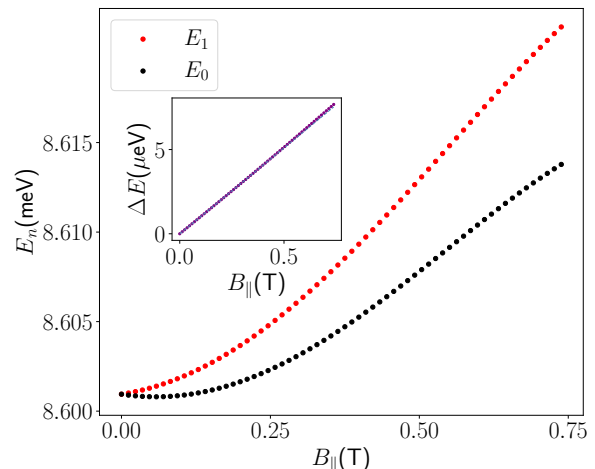


FIG. 3. Energy spectra of the lowest two spin states with an applied field in the [110] directions. The quantum dot is 40nm in radius with a germanium layer of 13nm in thickness and 20% of silicon in the barriers. The inset shows the corresponding energy difference (purple dotted) as well as the linear fit (blue dashed).

The total Hamiltonian of the quantum dot (1) can be written as a series expansion in the \mathbf{B} field [67], spin splitting is in general nonlinear in B field. For conduction electrons in quantum dots, the nonlinear contributions are too small to make a meaningful contribution in the operating regime of spin qubits. However, the situation seems to be different for holes. The strong HH-LH coupling can give rise to much stronger nonlinear-in- B contributions than the case of conduction electrons, because a typical Δ_{HL} is more than an order of magnitude smaller than the band gap in germanium. Nevertheless, we do not observe any nonlinear response to the B field in our system, at least in the current field range. Mathematically, the nonlinear contributions originate from orbital mixtures of the HH and the LH sub-bands, which depend inversely on Δ_{HL} . With the strain profile of Fig. 2 for the heterostructure we study, Δ_{HL} is large, thus the nonlinear contributions are almost negligible. One may expect a dramatic change of results if Δ_{HL} is much smaller.

B. Effect of quantum dot confinement

Considering the strength of spin-orbit coupling for holes, it is natural to expect that the confinement potential for the quantum dot will influence the hole spin splitting. The confinement potential for a planar quantum dot is described by three main parameters: the well width L_z along the growth direction, the silicon concentration α in the barrier, which determines the barrier height, and the in-plane dot size $L_{x,y}$ for the harmonic well. In this section, we explore these dependencies.

Figure 4(a) shows the in-plane g -factor for dot sizes of 40nm, 50nm, and 60nm with different in-plane directions of the applied field. Clearly, the effective g_{\parallel} is not sensitive to the dot size, and is nearly isotropic in the xy plane, even though the Burt-Foreman Hamiltonian (3) is known to have in-plane anisotropy arising from the HH-LH coupling. This coupling is suppressed by the large Δ_{HL} . When examined more closely, a small anisotropy can be seen in Fig. 5 on the effective g_{\parallel} in the [100] and [110] directions when the magnetic field is not small (the lower two panels).

As shown in Fig. 5, when the magnetic field is very small, g_{\parallel} is almost identical along the two directions; while a notable difference between the two directions appears when the orbital mixing is enhanced by a larger field. The difference is $\approx 1\%$ in the current setup of the planar dot, but can be significantly larger if Δ_{HL} is smaller. Another feature at the larger applied field is that g_{\parallel} in the [100] direction is clearly more sensitive to the change of well width compared to the [110] direction.

One of the distinct advantages of a finite barrier model is that it allows us to study the dependence of the g -factor on changing silicon concentration in the barrier. Recall that both the barrier heights and the uniaxial strain in the Ge well by lattice matching growth change with the percentage of silicon in the barriers. With increas-

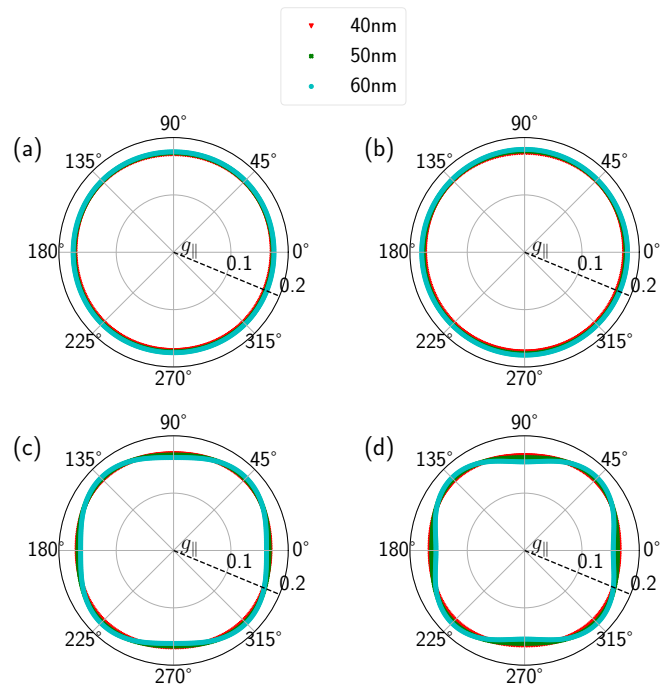


FIG. 4. Effective g_{\parallel} of a circular quantum dot with the Ge/GeSi heterostructure in four different conditions: (a) no electric field or residual tensile strain; (b) residual tensile strain that change 32% of the GeSi lattice constant; (c) a static electric field of 1MV/m in the growth direction; (d) combined effect of the residual tensile strain and the static electric field. Here 0° refers to the [100] direction. These results are calculated using the “shifted- m^* ” treatment of boundary conditions.

ing silicon concentration from 0.15 to 0.25, the effective g_{\parallel} becomes less sensitive to well width. Figure 5 also shows numerical results from the “fixed- m^* ” treatment of boundary conditions as a comparison. The two treatments show the same qualitative behavior in the current range of α , while a quantitative discrepancy is clear and increases with larger α .

C. g -factor in the growth direction

Along the growth direction for the Ge/GeSi heterostructure, the hole g -factor is known to be much larger compared to the in-plane direction, as the hole spin quantization axis is pinned to the growth direction by the quantum well confinement. Conversely, spin splitting in the quantum well along the growth direction should also be strongly affected by variations in the quantum well parameters. This observation is indeed clearly seen in our calculations. For example, Fig. 6 shows the effective g_{\perp} with varying silicon concentration and different well widths. The value of g_{\perp} is about two orders of magnitude larger than g_{\parallel} , leading to much larger spin splittings in general. Sensitivity of g_{\perp} to the dot size is still too small

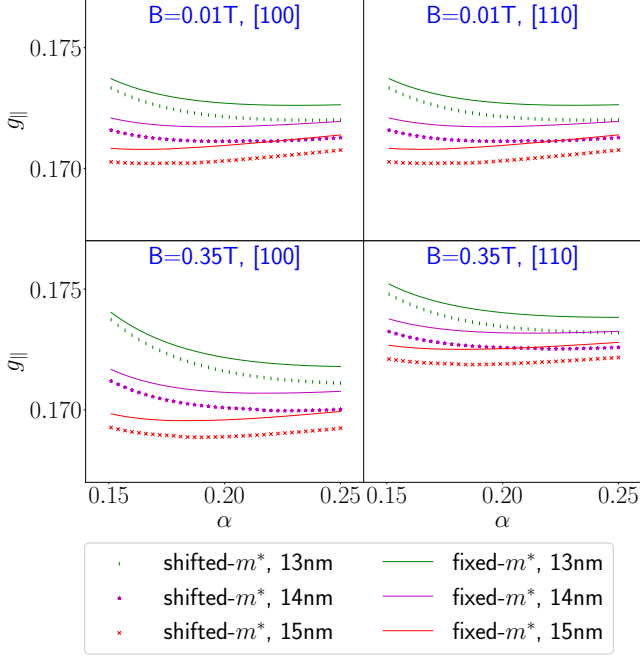


FIG. 5. Effective g_{\parallel} with varying silicon concentration and different well widths for a 40nm dot in a \mathbf{B}_{\parallel} field of (upper) 0.01 T; (lower) 0.35 T. The field is in the (left) [100] or (right) [110] directions.

to show. On the other hand, it is more sensitive to the well width, as expected. Similarly, g_{\perp} shows significant sensitivity to silicon concentration as well. This dependence is clearly not monotonic. The uptick of g_{\perp} at larger α is the result of a larger HH-LH splitting. In addition, the two treatments of boundary conditions show nearly identical qualitative behaviors with a constant shift of magnitude.

D. Analysis of the finite-barrier model

The two treatments of boundary conditions, which are only relevant for the finite barrier model we adopt, lead to non-negligible discrepancies in the calculations of g_{\parallel} and g_{\perp} . In essence, these two approaches yield a slight difference in the quantized momentum along the growth direction when solving for the out-of-plane component of the envelope function, therefore affecting the resulting spin-orbit coupling. Furthermore, the quantized momentum is also modified by varying the silicon concentration α in the barrier. Compared with the hard-wall model, where only Δ_{HL} is dependent on α , our more realistic model contains additional complexity, which in turn leads to different sensitivity of the effective g_{\parallel} and g_{\perp} to the choice of boundary conditions and the silicon concentration.

The different dependencies on the boundary conditions can be understood from the perspective of perturbation

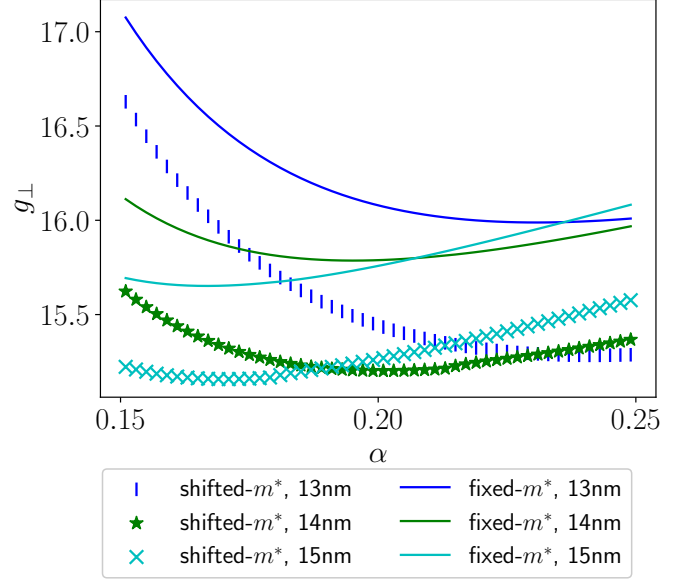


FIG. 6. The effective g_{\perp} as a function of α with different well widths of a 40nm dot. Sensitivity to well width increases with larger silicon concentration, while the disagreement between two treatments of boundary conditions is almost a constant in the whole range.

theory. The “unperturbed” in-plane g -factor provided by the Zeeman term is $g_{\parallel 0} = 0.18$. This Zeeman effect splits the $|\text{HH}+\rangle$ and $|\text{HH}-\rangle$ states, where we define

$$|\text{HH}+\rangle = \frac{1}{\sqrt{2}}(|\text{HH}\uparrow\rangle + |\text{HH}\downarrow\rangle), \quad (21)$$

$$|\text{HH}-\rangle = \frac{1}{\sqrt{2}}(|\text{HH}\uparrow\rangle - |\text{HH}\downarrow\rangle), \quad (22)$$

and similarly for the two LH states. The splitting between $|\text{LH}+\rangle$ and $|\text{LH}-\rangle$ is larger than the $|\text{HH}+\rangle$ - $|\text{HH}+\rangle$ splitting, as shown in Fig. 7 (left). According to perturbation theory, direct coupling between two states enhances their energy difference. This enhancement is larger when the two states are energetically closer to each other. Therefore, the $|\text{HH}+\rangle$ - $|\text{LH}+\rangle$ and $|\text{HH}-\rangle$ - $|\text{LH}-\rangle$ couplings (gray dashed) enhance the spin splitting of the HH states, while the $|\text{HH}+\rangle$ - $|\text{LH}-\rangle$ and $|\text{HH}-\rangle$ - $|\text{LH}+\rangle$ couplings (magenta dashed) decrease it. These two types of direct couplings counteract each other, reducing the sensitivity of the effective g_{\parallel} to the change of the quantized momentum. Therefore, the effective g_{\parallel} is not very sensitive to the choice of boundary conditions and to the silicon concentration.

On the other hand, the “unperturbed” out-of-plane g -factor $g_{\perp 0} \approx 21.27$. The out-of-plane B field splits $|\text{HH}\uparrow\rangle$ and $|\text{HH}\downarrow\rangle$ a lot more than it does to $|\text{LH}\uparrow\rangle$ and $|\text{LH}\downarrow\rangle$, as shown in fig. 7 (right). Both direct coupling mechanisms (gray dashed and magenta dashed) reduce the HH spin splitting. Therefore, this splitting will be more sensitive to the change of k_z , thus to the choice of

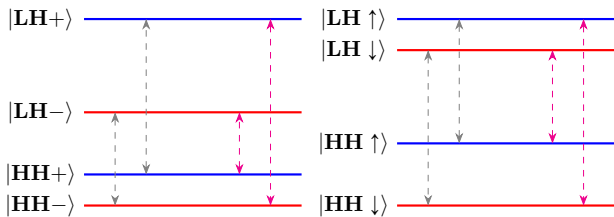


FIG. 7. Schematic representation of the HH-LH coupling with an (left) in-plane or (right) out-of-plane magnetic field.

boundary conditions as well as to the silicon concentration.

The above analysis is based on a relatively large HH-LH splitting so that direct couplings play the most important role. A more complicated situation arises if the HH and LH bands are closer to each other. The non-negligible high-order terms can also contribute to changes in g_{\parallel} and g_{\perp} , leading to larger discrepancies between the two treatments of boundary conditions, and a more dramatic sensitivity to confinement parameters of the system.

E. Electric field in the growth direction

For a planar quantum dot in a Ge quantum dot, the in-plane confinement is produced by top gates that are charged. In addition to providing in-plane confinement, the charged gates also produce a static electric field in the growth direction:

$$H_Z = eF_z z. \quad (23)$$

This static electric field induces a Rashba-type spin-orbit coupling by breaking the inversion symmetry of the square well. A systematic study of the effective g -factor for a confined hole should thus consider the effect of this electric field.

Figure 8 shows the in-plane g -factor of a 40nm dot with a well width of 13nm. With the electric field increased to 1MV/m, the anisotropic nature of our Hamiltonian becomes clearer. The [100] direction g -factor has a larger sensitivity to the electric field, such that a 1MV/m field can decrease its value by $\approx 4.5\%$, while along the [110] direction, the reduction is $\approx 1.6\%$.

However, the static electric field along z direction has a minimal impact on the g -factor along that direction, g_{\perp} . This insensitivity is not really surprising: the out-of-plane magnetic field has already broken the symmetry of the square well by splitting the left-circular and the right-circular orbitals. A further splitting by an electric field thus can only have a limited effect on the spin splitting: about 0.6% decrease in the g_{\perp} value by increasing the E field from 0 to 1MV/m.

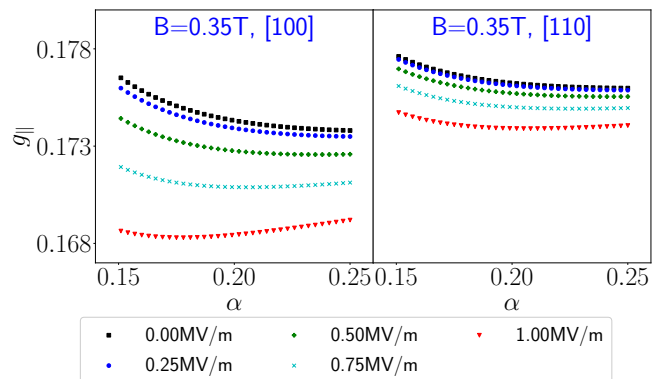


FIG. 8. Effective g_{\parallel} with the “shifted- m^* ” method of a 40nm dot with a well width of 13nm. The static electric field is applied in the growth direction with different magnitudes. The difference between g_{\parallel} in the [100] and the [110] directions is getting larger as the strength of the electric field increases.

F. Residual tensile strain

The above calculations are based on Fig. 2 with the assumption that both $\text{Ge}_{1-\alpha}\text{Si}_{\alpha}$ barriers are fully relaxed, while the Ge layer is grown lattice-matched to the relaxed $\text{Ge}_{1-\alpha}\text{Si}_{\alpha}$ and is thus compressively strained so that it acts as a quantum well for the holes. Recall that the heterostructure of our concern is grown at finite temperature on a silicon substrate. When cooled down to the experimental temperature in the order of tens of mK, the difference in thermal contraction between Si and Ge leads to a residual tensile strain in the in-plane direction in the $\text{Ge}_{1-\alpha}\text{Si}_{\alpha}$ barrier [68, 69], which in turn reduces the compressive stress it applies on the Ge well. Consequently, the residual tensile strain splits the HH and LH bands in the barriers at the Brillouin zone center and reduces the HH-LH splitting inside the Ge well.

Here we introduce the ratio $\delta a_0/\Delta a_0[\text{GeSi}]$ as in Eq. (B7) of Appendix B to represent the residual strain in the barrier. The set of strain elements by most of the studies in the literature is in the range of $\delta a_0/\Delta a_0[\text{GeSi}] = 30\% \sim 32\%$ in our calculations. Nevertheless, we vary the residual strain from 0 to 40 percent to evaluate its impact on spin splitting. Based on our calculations, the in-plane g -factor changes only minimally, while the out-of-plane g -factor is more sensitive to the residual strain, as shown in Fig. 9. In the realistic case of 32% change of lattice constant, the effective g_{\perp} has a reduction of $\approx 8\%$ compared with the ideal case of fully relaxed barriers.

G. Combined effects on the in-plane anisotropy

In a realistic Ge/GeSi heterostructure, both residual strain and z direction electric field are present. The combination helps enhance spin-orbit interaction for the con-

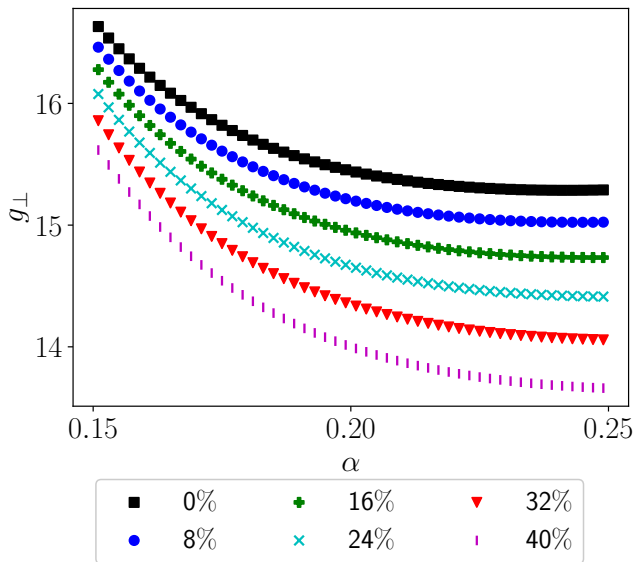


FIG. 9. Effective g_{\perp} with the “shifted- m^* ” method of a 40nm dot with a well width of 13nm. The electric field is set to 0 because it has a minimal impact. The residual strain in the barrier shifts the g_{\perp} vs. α curves downward as it gets larger.

finer hole. Figure 4(b) shows the effective g_{\parallel} in the whole x - y plane affected by residual tensile strain that changes the GeSi lattice constant by 32%. The result is slightly more sensitive to the dot size compared with the ideal model counterpart 4(a). However, when a static electric field is applied, the same amount of residual strain will enhance the sensitivity to the dot size more notably, as seen by comparing panels (c) and (d) of Figs. 4.

IV. CONCLUSION AND DISCUSSION

We have studied spin splitting of the ground Kramers doublet in a planar Ge quantum dot with a magnetic field in the in-plane or out-of-plane direction. We adopted a realistic model of finite barriers in the growth direction and performed self-consistent calculations. Boundary conditions with or without a sudden change in effective mass across the barrier are compared. We find that in an ideal model of a circular planar dot in a square-well heterostructure with two fully relaxed barriers, the qubit spin splitting has a relatively weak dependence on confinement parameters, especially for the g -factor in the in-plane direction. Our results indicate that the effective spin-orbit coupling of such a system may not be large enough for fast electrical control. On the other hand, realistic experimental effects, including the top-gate electric field and the residual strain in the barriers, will both enhance the effective spin-orbit coupling.

Our results show that there is often a non-negligible discrepancy between our two choices of boundary condi-

tions on the effective mass, which should be considered when optimizing the qubit. While it seems more appropriate to include the change of effective mass in boundary conditions, our calculations provide benchmarks for the two treatments, and emphasize an underlying uncertainty of the formalism. Experimental measurements will have to be the ultimate judge on which approach is the better reflection of the reality. Qualitatively, in the treatment of such heterostructures, the $\mathbf{k} \cdot \mathbf{p}$ formalism assumes a global lattice periodicity, which contradicts the change of material properties in different layers. In fact, such a contradiction arises from the effective-mass approximation of a few-band model. If we start with the free-electron mass and use a large enough set of bands to perform $\mathbf{k} \cdot \mathbf{p}$ calculation, the ambiguity of boundary conditions should disappear. But this is computationally challenging and might be better suited for first-principle calculations.

Within the $\mathbf{k} \cdot \mathbf{p}$ formalism, gauge invariance could be another feature where contradiction arises. If we start with the lattice Lagrangian and derive the equation of motion, gauge invariance should be preserved in the system. However, the $\mathbf{k} \cdot \mathbf{p}$ formalism neglects the effect of the vector potential on the Bloch states. In this case, gauge invariance may *in principle* not be preserved for the total effective mass Hamiltonian (1). The problem of gauge invariance arises because of the HH-LH coupling in the $\mathbf{k} \cdot \mathbf{p}$ Hamiltonian. When the splitting between HH and LH bands is large, the system shows reasonable gauge invariance in the weak-field limit ($B \approx 0$ T) by comparing the Landau gauge and the symmetric gauge in x - y directions, as pointed out in [70]. However, when the applied field is as large as $B = 0.35$ T, a clear discrepancy (5~10%) between two gauges is observed. This discrepancy can be significantly enhanced if the HH-LH splitting is much smaller.

In other words, the actual gauge-invariant Hamiltonian contains terms beyond the scope of the current effective mass Hamiltonian derived in the $\mathbf{k} \cdot \mathbf{p}$ formalism. This problem can potentially also be addressed by first-principle calculations. The present calculations are carried out with a symmetric gauge because it contributes in different directions evenly.

Another important aspect of the present treatment is the accuracy of the LCAO technique. The truncation of the number of sub-bands could limit the accuracy of the energy eigenstates for the system. A given finite well does not have an infinite number of sub-bands. In our numerical calculation, such a truncated basis set may not be able to reproduce the true eigenstates of the system. A pragmatic improvement is to use two hard-wall caps outside the finite barriers in order to discretize the continuous scattering states and include their effects in the calculations, as done in [47]. The present work can be viewed as the starting point for the long-term goal of finding a viable way to avoid the hard-wall approximation for the study of more complicated quantum dot architectures.

This paper aims to facilitate the engineering of GeSi alloy for a reliable Ge qubit. In Ge/GeSi heterostructure, an adequate treatment of the realistic valence-band offset can help better understand how confining layers affect qubit properties. The dependence of the qubit spin splitting on silicon concentration shows a possible magnitude of noise coming from the alloy manufacturing. On the other hand, varying silicon concentration can also change the sensitivity of the g -factor to the confinement. This sensitivity is not monotonic with the percentage of silicon in the barriers, and therefore, can be explored both theoretically and experimentally. The engineering of confining alloys is thus another degree of freedom for reliable qubits. Stability of qubit properties is wanted even with imperfections in the manufacturing process. Predictable operating conditions are desired, including dopant con-

centration. In addition, this work assumed an alloy with evenly distributed Si and Ge, which is an ideal assumption. Effect of disorders in the actual alloys may be a fruitful direction of future research.

ACKNOWLEDGMENTS

We acknowledge financial support from the UB CAS Dean's Office. HFF thanks support from the National Science Foundation under grant NSF PHY-2014023 and NSF OAC-1931367, and XH thanks support from US AFOSR through grant FA9550-23-1-0710 and US ARO through grant W911NF2310018. We also thank the valuable discussions with Dimitrie Culcer's group at UNSW in Sydney, Australia, and Maximilian Russ' group at TU Delft in Delft, Netherlands.

Appendix A: A sign difference in the Burt-Foreman Hamiltonian

The different sign in our Burt-Foreman Hamiltonian eq.(3) compared to the original one by Foreman [53] comes from the use of zone-center basis states. If we use the standard $|j, j_z\rangle$ states for $j = 3/2$, the matrix representations of \mathbf{J} components are

$$J_x = \begin{pmatrix} 0 & \frac{\sqrt{3}}{2} & 0 & 0 \\ \frac{\sqrt{3}}{2} & 0 & 1 & 0 \\ 0 & 1 & 0 & \frac{\sqrt{3}}{2} \\ 0 & 0 & \frac{\sqrt{3}}{2} & 0 \end{pmatrix}, \quad J_y = \begin{pmatrix} 0 & -i\frac{\sqrt{3}}{2} & 0 & 0 \\ i\frac{\sqrt{3}}{2} & 0 & -i & 0 \\ 0 & i & 0 & -i\frac{\sqrt{3}}{2} \\ 0 & 0 & i\frac{\sqrt{3}}{2} & 0 \end{pmatrix}, \quad J_z = \begin{pmatrix} \frac{3}{2} & 0 & 0 & 0 \\ 0 & \frac{1}{2} & 0 & 0 \\ 0 & 0 & -\frac{1}{2} & 0 \\ 0 & 0 & 0 & -\frac{3}{2} \end{pmatrix}. \quad (\text{A1})$$

The p -like orbital states $|l, l_z\rangle$, on the other hand, are defined as linear combinations of $|X\rangle$, $|Y\rangle$, $|Z\rangle$, [71]

$$\begin{aligned} |1, 1\rangle &= -\frac{1}{\sqrt{2}}|X + iY\rangle, \\ |1, 0\rangle &= |Z\rangle, \\ |1, -1\rangle &= \frac{1}{\sqrt{2}}|X - iY\rangle. \end{aligned} \quad (\text{A2})$$

Then, we can evaluate all $|j, j_z\rangle$ states in the $|l, l_z; s, s_z\rangle$ basis by calculating all the Clebsch-Gordan coefficients. We end up with

$$\begin{aligned} |3/2, 3/2\rangle &= -\frac{1}{\sqrt{2}}|(X + iY), \uparrow\rangle, \\ |3/2, 1/2\rangle &= -\frac{1}{\sqrt{6}}|(X + iY), \downarrow\rangle + \sqrt{\frac{2}{3}}|Z, \uparrow\rangle, \\ |3/2, -1/2\rangle &= \frac{1}{\sqrt{6}}|(X - iY), \uparrow\rangle + \sqrt{\frac{2}{3}}|Z, \downarrow\rangle, \\ |3/2, -3/2\rangle &= \frac{1}{\sqrt{2}}|(X - iY), \downarrow\rangle. \end{aligned} \quad (\text{A3})$$

Deriving the Burt-Foreman model with such a basis, we will eventually get (3) and (4). Giving a global phase to the basis states (A3) doesn't change the matrix representation. However, Foreman's basis states are not in a consistent phase with (A3). It is still a complete basis which doesn't affect the calculation of bulk or heterostructure properties, but it can cause non-negligible error in qubit Zeeman splitting if H_{BF} and \mathbf{J} are not in the same basis.

Appendix B: Material properties

The Foreman parameters are defined as $\bar{\gamma} = (\gamma_2 + \gamma_3)/2$, $\mu = (\gamma_3 - \gamma_2)/2$, $\delta = (1 + \gamma_1 + \gamma_2 - 3\gamma_3)/9$, $\sigma = \bar{\gamma} - \delta/2$, $\pi = \mu + 3\delta/2$.

For all the material parameters, we followed [72] and the supplemental material of [70] to calculate them with *linear interpolation*. The strain tensor has only diagonal terms for uniaxial strain. In our calculations,

$$\varepsilon_{xx} = \varepsilon_{yy} = \frac{\Delta a_0^2}{2a_0^2}, \quad (\text{B1})$$

and $\varepsilon_{zz} = -\frac{2c_{12}}{c_{11}}\varepsilon_{xx}$ [45, 47]. Here Δa_0 is the difference of lattice constant between GeSi and Ge, and Vegard's law is used to calculate the lattice constant of GeSi

$$a_0[\text{Ge}_{1-\alpha}\text{Si}_\alpha] = a_0[\text{Ge}](1 - \alpha) + a_0[\text{Si}]\alpha - 0.027\alpha(1 - \alpha), \quad (\text{B2})$$

as well as the variance

$$\Delta a_0^2 = a_0^2[\text{Ge}_{1-\alpha}\text{Si}_\alpha] - a_0^2[\text{Ge}]. \quad (\text{B3})$$

	$a_0(\text{\AA})$	γ_1	γ_2	γ_3	$a_v(\text{eV})$	$b_v(\text{eV})$	$c_{11}(\text{GPa})$	$c_{12}(\text{GPa})$	κ	q	$V_0(\text{eV})$
Ge	5.658	13.380	4.240	5.690	2.00	-2.160	131.0	49.0	3.410	0.060	-
Si	5.430	4.285	0.339	1.446	2.10	-2.330	167.5	64.9	-0.420	0.010	-
$\text{Ge}_{0.85}\text{Si}_{0.15}$	5.620	12.016	3.655	5.053	2.015	-2.186	136.5	51.4	2.836	0.053	0.104
$\text{Ge}_{0.8}\text{Si}_{0.2}$	5.608	11.561	3.460	4.841	2.02	-2.194	138.3	52.2	2.644	0.050	0.132
$\text{Ge}_{0.75}\text{Si}_{0.25}$	5.596	11.106	3.265	4.629	2.025	-2.203	140.1	53.0	2.453	0.048	0.156

TABLE I. Material properties of the Ge/GeSi heterostructure.

The barrier height V_0 is determined by the valence-band offset ΔE^v of the heterostructure. A theoretical prediction of strained Ge on a relaxed substrate of $\text{Ge}_{1-\alpha}\text{Si}_\alpha$ alloy is [73]

$$\Delta E^v(\alpha) = \alpha[0.6 - 0.7(2 - \alpha)]\text{eV}. \quad (\text{B4})$$

The calculation of strain tensor is based on eq. (B1). The difference is both the Ge layer and the two GeSi alloys will have variances.

$$\Delta a_0^2[\text{Ge}] = a_0^{*2} - a_0^2[\text{Ge}], \quad (\text{B5})$$

$$\Delta a_0^2[\text{GeSi}] = a_0^{*2} - a_0^2[\text{GeSi}], \quad (\text{B6})$$

where a_0^* is the lattice constant of the heterostructure. For convenience, we define the change of lattice constant from the $a_0[\text{GeSi}]$ as

$$\delta a_0/\Delta a_0[\text{GeSi}] = (a_0^* - a_0[\text{GeSi}])/(a_0[\text{Ge}] - a_0[\text{GeSi}]). \quad (\text{B7})$$

In table II, we show all the elements of the strain tensor in the case where there is 20% silicon in the barriers.

$\delta a_0/\Delta a_0[\text{Ge}_{0.8}\text{Si}_{0.2}]$	$a_0^*(\text{\AA})$	$\varepsilon_{ }[\text{Ge}]$	$\varepsilon_{zz}[\text{Ge}]$	$\varepsilon_{ }[\text{Ge}_{0.8}\text{Si}_{0.2}]$	$\varepsilon_{zz}[\text{Ge}_{0.8}\text{Si}_{0.2}]$
0%	5.608	-0.878%	0.657%	0%	0%
8%	5.612	-0.808%	0.605%	0.071%	-0.054%
16%	5.616	-0.738%	0.552%	0.143%	-0.108%
24%	5.620	-0.668%	0.500%	0.214%	-0.161%
32%	5.624	-0.598%	0.447%	0.285%	-0.215%
40%	5.628	-0.528%	0.395%	0.357%	-0.269%

TABLE II. Elements of the strain tensor for the Ge/Ge_{0.8}Si_{0.2} heterostructure with different changes of lattice constant in the barrier.

Appendix C: Coupling of in-plane states with different effective masses

The electrostatic confinement generates the same harmonic potential for energy bands 1 and 2 of a single particle

$$V_{\parallel}(x) = \frac{1}{2}m_1\omega_1x^2 = \frac{1}{2}m_2\omega_2x^2, \quad (\text{C1})$$

where $m_{1(2)}$, $\omega_{1(2)}$ are effective mass and frequency of band 1(2). The effective confinement size $L_{1(2)} = \sqrt{\hbar/(m_{1(2)}\omega_{1(2)})}$ should be different if such a particle has different effective masses in these two bands. In this case, the corresponding wave functions ψ_{1n} , ψ_{2m} will not follow the orthonormal property $\langle\psi_{1n}|\psi_{2m}\rangle = \delta_{nm}$. Thus, additional care must be taken when evaluating the matrix representation of terms coupling the two bands. Here, we provide an analytical benchmark for the calculation of matrix elements.

1. Harmonic oscillators

In the harmonic oscillator basis, the wave function is in the form

$$\psi_{1(2)n} = \frac{1}{\sqrt{2^n n!}} \left(\frac{1}{\pi L_{1(2)}^2} \right)^{\frac{1}{4}} e^{-\frac{x^2}{2L_{1(2)}^2}} H_n \left(\frac{x}{L_{1(2)}} \right). \quad (\text{C2})$$

One then needs to evaluate the integral

$$\langle\psi_{1n}|\psi_{2m}\rangle = \frac{1}{\sqrt{2^{n+m} n! m!}} \left(\frac{1}{\pi L_1 L_2} \right)^{\frac{1}{2}} \int dx e^{-\frac{x^2}{2L_1^2} - \frac{x^2}{2L_2^2}} H_n \left(\frac{x}{L_1} \right) H_m \left(\frac{x}{L_2} \right), \quad (\text{C3})$$

where $L_1 \neq L_2$. This integral can be evaluated using the explicit expression of Hermite polynomials

$$H_n(x) = n! \sum_{l=0}^{\lfloor \frac{n}{2} \rfloor} \frac{(-1)^l}{l!(n-2l)!} (2x)^{n-2l}, \quad (\text{C4})$$

where $\lfloor n \rfloor$ is a floor function of n . With a change of variables, we eventually need to evaluate an integral of the form

$$\int du e^{-u^2} H_n(au) H_m(bu), \quad (\text{C5})$$

where the coefficients a , b are

$$a = \frac{\sqrt{2}L_2}{\sqrt{L_1^2 + L_2^2}}, \quad b = \frac{\sqrt{2}L_1}{\sqrt{L_1^2 + L_2^2}}, \quad (\text{C6})$$

and the new variable

$$u = \frac{\sqrt{L_1^2 + L_2^2}}{\sqrt{2}L_1 L_2} x. \quad (\text{C7})$$

Applying a useful integral

$$\mathcal{I}(n, m, r, s) = \int_{-\infty}^{\infty} e^{-u^2} u^{n+m-2r-2s} du = \frac{\Gamma\left(\frac{n}{2} + \frac{m}{2} - r - s + \frac{1}{2}\right) (1 + (-1)^{n+m})}{2}, \quad (\text{C8})$$

we can eventually get the expression of the coupling integral (C3) in a closed form

$$\langle\psi_{1n}|\psi_{2m}\rangle = \frac{1}{\sqrt{2^{n+m} n! m!}} \left(\frac{1}{\pi} \right)^{\frac{1}{2}} \frac{\sqrt{2}L_1 L_2}{\sqrt{L_1^2 + L_2^2}} n! m! 2^{n+m} \sum_{r=0}^{\lfloor \frac{n}{2} \rfloor} \sum_{s=0}^{\lfloor \frac{m}{2} \rfloor} \frac{(-1)^{r+s} 2^{-2r-2s}}{r!(n-2r)!s!(m-2s)!} a^{n-2r} b^{m-2s} \mathcal{I}(n, m, r, s). \quad (\text{C9})$$

2. Fock-Darwin states

In the Fock-Darwin basis, we need to deal with a similar integral. The general expression of circular Fock-Darwin state is

$$\psi_{nm}(\rho, \phi) = NR_n(\rho)e^{im\phi}, \quad (\text{C10})$$

Here n is the principal quantum number of the Fock-Darwin states $n = n_+ + n_-$, and m is the magnetic quantum number $m = n_+ - n_-$, with N the normalization factor, and $R_n(\rho)$ the radial part of the wave function. A useful quantum number n_r is defined as $n_r = (n - |m|)/2$ for the radial function

$$R_n(\rho) = \sqrt{\frac{2n_r!}{(n_r + |m|)!}} \left(\frac{\rho}{L_b}\right)^{|m|} e^{-\frac{\rho^2}{2L_b^2}} \mathcal{L}_{n_r}^{|m|} \left(\frac{\rho^2}{L_b^2}\right), \quad (\text{C11})$$

where $\mathcal{L}_{n_r}^{|m|}$ is the associated Laguerre polynomial that has a closed form

$$\mathcal{L}_{n_r}^{|m|}(x) = \sum_{i=0}^{n_r} (-1)^i \binom{n_r + |m|}{n_r - i} \frac{x^i}{i!}. \quad (\text{C12})$$

Normalization of the wave function

$$|N|^2 2\pi \int_0^\infty \frac{n_r!}{(n_r + |m|)!} \left(\frac{\rho^2}{L_b^2}\right)^{|m|} e^{-\frac{\rho^2}{L_b^2}} \left[\mathcal{L}_{n_r}^{|m|} \left(\frac{\rho^2}{L_b^2}\right)\right]^2 d\rho^2 = |N|^2 2\pi L_b^2 = 1 \quad (\text{C13})$$

can lead to

$$N = \frac{1}{\sqrt{2\pi} L_b}.$$

The effective confinement L_b is determined similarly to the case of the harmonic oscillator and thus varies with the effective masses. We will end up with a similar coupling integral

$$\begin{aligned} & \int_0^{2\pi} \int_0^\infty \psi_{n_1 m_1}^*(\rho, \phi) \psi_{n_2 m_2}(\rho, \phi) \rho d\rho d\phi = \frac{1}{2\pi L_{b1} L_{b2}} \int_0^{2\pi} e^{i(m_2 - m_1)\phi} d\phi \int_0^\infty R_{n_1, n_1}^*(\rho) R_{n_2, n_2}(\rho) \rho d\rho \\ &= \frac{1}{2L_{b1} L_{b2}} \int_0^\infty \sqrt{\frac{4n_{1r}! n_{2r}!}{(n_{1r} + |m|)! (n_{2r} + |m|)!}} \left(\frac{\rho^2}{L_{b1} L_{b2}}\right)^{|m|} e^{-\frac{\rho^2}{2L_{b1}^2} - \frac{\rho^2}{2L_{b2}^2}} \mathcal{L}_{n_{1r}}^{|m|} \left(\frac{\rho^2}{L_{b1}^2}\right) \mathcal{L}_{n_{2r}}^{|m|} \left(\frac{\rho^2}{L_{b2}^2}\right) d\rho^2 \\ &= \sqrt{\frac{n_{1r}! n_{2r}!}{(n_{1r} + |m|)! (n_{2r} + |m|)!}} (L_{b1} L_{b2})^{-|m|-1} \int_0^\infty \rho^{2|m|} e^{-\frac{\rho^2}{2L_{b1}^2} - \frac{\rho^2}{2L_{b2}^2}} \mathcal{L}_{n_{1r}}^{|m|} \left(\frac{\rho^2}{L_{b1}^2}\right) \mathcal{L}_{n_{2r}}^{|m|} \left(\frac{\rho^2}{L_{b2}^2}\right) d\rho^2 \\ &= \sqrt{\frac{n_{1r}! n_{2r}!}{(n_{1r} + |m|)! (n_{2r} + |m|)!}} (L_{b1} L_{b2})^{-|m|-1} \sum_{i=0}^{n_{1r}} \sum_{j=0}^{n_{2r}} \frac{(-1)^{i+j}}{i! j!} \binom{n_{1r} + |m|}{n_{1r} - i} \binom{n_{2r} + |m|}{n_{2r} - j} \\ &\times \int_0^\infty \rho^{2|m|} e^{-\frac{\rho^2}{2L_{b1}^2} - \frac{\rho^2}{2L_{b2}^2}} \left(\frac{\rho^2}{L_{b1}^2}\right)^i \left(\frac{\rho^2}{L_{b2}^2}\right)^j d\rho^2 \\ &= \sqrt{\frac{n_{1r}! n_{2r}!}{(n_{1r} + |m|)! (n_{2r} + |m|)!}} \sum_{i=0}^{n_{1r}} \sum_{j=0}^{n_{2r}} \frac{(-1)^{i+j}}{i! j!} \binom{n_{1r} + |m|}{n_{1r} - i} \binom{n_{2r} + |m|}{n_{2r} - j} \\ &\times (L_{b1})^{2j+|m|+1} (L_{b2})^{2i+|m|+1} 2^{i+j+|m|+1} (L_{b1}^2 + L_{b2}^2)^{-1-i-j-|m|} \Gamma(i+j+|m|+1). \end{aligned} \quad (\text{C14})$$

Appendix D: Quantum well sub-bands with the coupled boundary conditions

Generally, the total envelope function constructed by single-band envelope functions

$$|\Psi\rangle = \sum_{j_z} \sum_{lmn} |\psi_{j_z}^{mn}(x, y) \phi_{j_z}^l(z)\rangle \quad (\text{D1})$$

does not satisfy the coupled boundary conditions. Here we introduce a treatment to modify the quantum-well envelope functions. The idea is: if each basis state $|\phi(z)\rangle$ satisfies the coupled boundary conditions, the total envelope function constructed by these states should satisfy the same boundary conditions automatically. This treatment is to estimate the correction to the quantum well sub-bands by using different boundary conditions. For convenience, we apply this treatment to the Luttinger-Kohn Hamiltonian in order to avoid the complication of LH-LH coupling. In this case, the derivative operator \mathcal{D} can be reduced to the 2×2 form in the $||3/2\rangle, ||1/2\rangle$ representation

$$\mathcal{D}_{\text{LK}}^{2 \times 2} = \begin{pmatrix} (\gamma_1 - 2\gamma_2) \frac{\partial}{\partial z} & -i\sqrt{3}\gamma_3(k_x - ik_y) \\ i\sqrt{3}\gamma_3(k_x + ik_y) & (\gamma_1 + 2\gamma_2) \frac{\partial}{\partial z} \end{pmatrix} \quad (\text{D2})$$

We now assume the quantum well sub-bands are in the form of HH-LH mixture. For example, the even HH sub-bands can be in the form

$$|\phi_{hw}(z)\rangle = \begin{pmatrix} A_{h1} \cos(k_h z) \\ A_{h2} \sin(k_h z) \end{pmatrix}, \quad |\phi_{hb}(z)\rangle = \begin{pmatrix} B_{h1} e^{\pm\chi_h z} \\ B_{h2} e^{\pm\chi_h z} \end{pmatrix}. \quad (\text{D3})$$

Component in the $||3/2\rangle$ band, $A_{h1} \cos(k_h z)$ in the well and $B_{h1} e^{\pm\chi_h z}$ in the barrier, is the ‘‘main’’ state. The corresponding component in the $||1/2\rangle$ band is then the ‘‘mixture’’. This means, for each eigenmode k_h (χ_h) in the HH band, there is a coupling to the LH band with an opposite parity. This state should satisfy the continuity of envelope function in each channel (14), and the matrix equation

$$\begin{pmatrix} (\gamma_1^{(w)} - 2\gamma_2^{(w)}) \frac{\partial}{\partial z} & -i\sqrt{3}\gamma_3^{(w)}(k_x - ik_y) \\ i\sqrt{3}\gamma_3^{(w)}(k_x + ik_y) & (\gamma_1^{(w)} + 2\gamma_2^{(w)}) \frac{\partial}{\partial z} \end{pmatrix} |\phi_{hw}\rangle = \begin{pmatrix} (\gamma_1^{(b)} - 2\gamma_2^{(b)}) \frac{\partial}{\partial z} & -i\sqrt{3}\gamma_3^{(b)}(k_x - ik_y) \\ i\sqrt{3}\gamma_3^{(b)}(k_x + ik_y) & (\gamma_1^{(b)} + 2\gamma_2^{(b)}) \frac{\partial}{\partial z} \end{pmatrix} |\phi_{hb}\rangle. \quad (\text{D4})$$

On the other hand, applying the uncoupled Hamiltonian of quantum well to sub-band states (D4)

$$\left(-\frac{\hbar^2}{2m_{\perp}^{h(l)}} \frac{\partial^2}{\partial z^2} + V_{\text{eff}}^{h(l)}(z) \right) |\phi_{h(l)}(z)\rangle = E^{h(l)} |\phi_{h(l)}(z)\rangle \quad (\text{D5})$$

leads to the same energy equation (16), where $m_{\perp}^{h(l)}$, $V_{\text{eff}}^{h(l)}(z)$ and $E^{h(l)}$ refer to the heavy-hole (light-hole) effective mass, effective barrier and sub-band energy in the quantum well.

The solutions of these equations are modified finite-well sub-bands. They do not refer to any physical states because the uncoupled Hamiltonian and the matrix equation (D4) are not consistent with each other. Instead, they are artificial states in order to construct the total envelope function required by the coupled boundary conditions.

Table III shows how large the mixture amplitude is compared to its main state, for example, $|A_{h2}/A_{h1}|$ for (D3). The quantum well is set to be 10nm wide and the in-plane wave vector is 0.002 \AA^{-1} (inverse of a 50nm confinement) with 20% silicon in the barrier. We can see the correction to the envelope function is very small; thus, the correction to energy is almost negligible. However, the correction can be significant if the in-plane confinement is comparable to the out-of-plane confinement.

	$ A_{\text{mixture}}/A_{\text{main}} $
HH1	0.07%
HH2	0.14%
HH3	0.19%
LH1	1.47%
LH2	2.52%

TABLE III. Mixture amplitude as a percentage of its main state in a Ge/Ge_{0.8}Si_{0.2} heterostructure.

This artificial treatment to the coupled boundary conditions was not applied to the g -factor calculations because it is more of a trial to address the coupled boundary conditions within the LCAO technique. In an accurate quantum dot calculation, the in-plane wave vectors cannot even be treated as numbers, so one must modify in-plane and out-of-plane sub-bands simultaneously, and it is computationally challenging.

Appendix E: Spin splitting with a different HH-LH splitting

The purpose of this section is to explore the theoretical possibility of the HH-LH splitting, Δ_{HL} , being smaller. Here we consider the scenario of the germanium layer being relaxed while the two GeSi barriers are strained by the

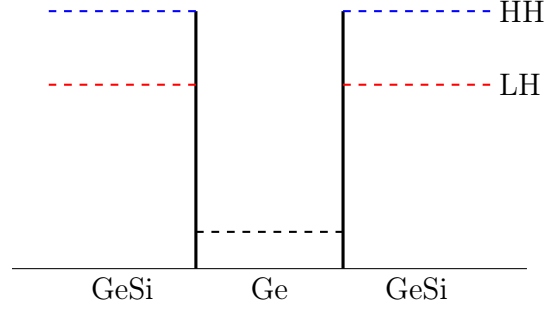


FIG. 10. A fictitious band alignment of the Ge/GeSi heterostructure if the GeSi barriers are strained and the Ge layer is relaxed.

lattice matching mechanism. The resulting band alignment will be as pictured in Fig. 10. Comparing the results of this scenario to the realistic case, we can see how the size of Δ_{HL} affects the qubit Zeeman splitting. Therefore, we reproduced the same type of calculations with these assumptions.

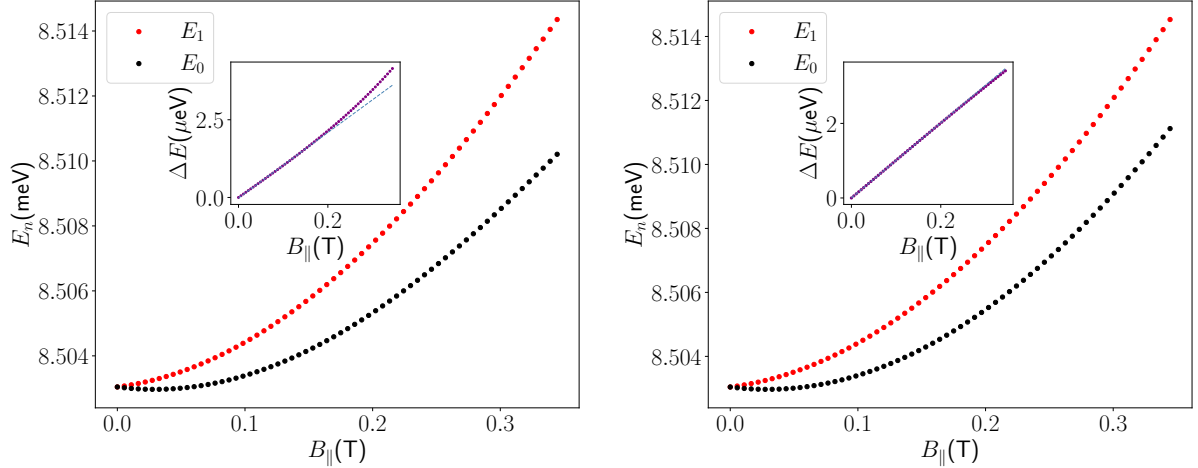


FIG. 11. Energy spectra of the same setup of quantum dot as Fig. 3 in a different strain paradigm with an applied field in the (left) [100] and (right) [110] directions. Nonlinear behavior can already be seen for the spin splitting when the field is in the [100] direction with a magnitude larger than 0.2 T.

The energy spectra in Fig. 12 show an obvious nonlinear splitting if the applied magnetic field is in the [100] direction when the field is larger than 0.2 T. The nonlinear effect is less dramatic in the [110] direction, and thus, a strong anisotropy in the x - y plane can be expected, as shown in the left plot of Fig. 12, where we applied a 0.35 T in-plane field. Here we abandoned the concept of “effective g -factor” but showed energy splitting instead because we no longer have a field-independent g -factor.

The in-plane anisotropy is clearly sensitive to the size of the dot, where a larger dot has a stronger anisotropy. From the right plot of Fig. 12, we can see the nonlinear effect can change dramatically how the well width affects the spin splitting. It also increases the sensitivity to the well width as well as the discrepancy between the two treatments of boundary conditions.

The stronger HH-LH coupling reduces the value of g_{\perp} . Compared with the original paradigm, the effective g_{\perp} becomes less sensitive to well width with the increase of silicon concentration. Other than that, the value of g_{\perp} seems to converge to a certain value with growing α . The reason is that the HH-LH splitting comes exclusively from the different energies of the lowest sub-bands of HH and LH. As α increases, the quantum wells of HH and LH will become closer and closer to the hard-wall scenario.

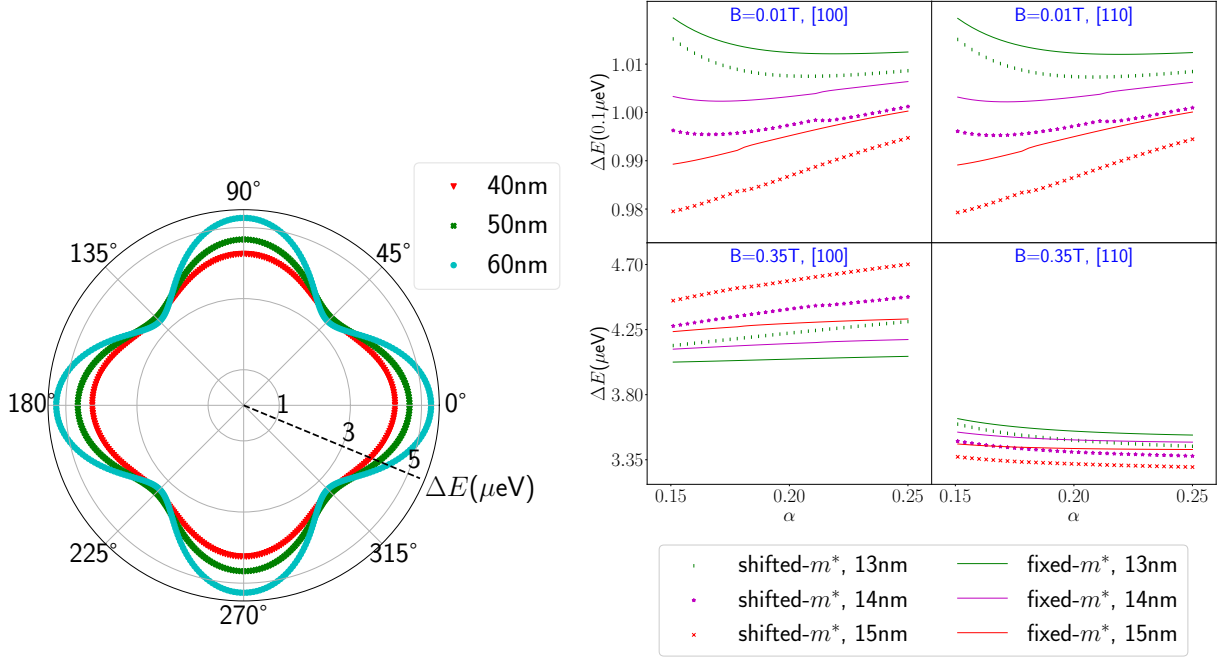


FIG. 12. (Left) Spin splitting of a dot with a 13-nm-wide quantum well and an in-plane magnetic field applied in all different directions. The [100] direction is when $\theta = 0^\circ$. (Right) Spin splitting of a 40nm dot as a function of silicon concentration α in the [100] and [110] directions. Results include the weak-field limit (0.01T) and a regular B field (0.35T), with three different well widths, in two treatments of boundary conditions.

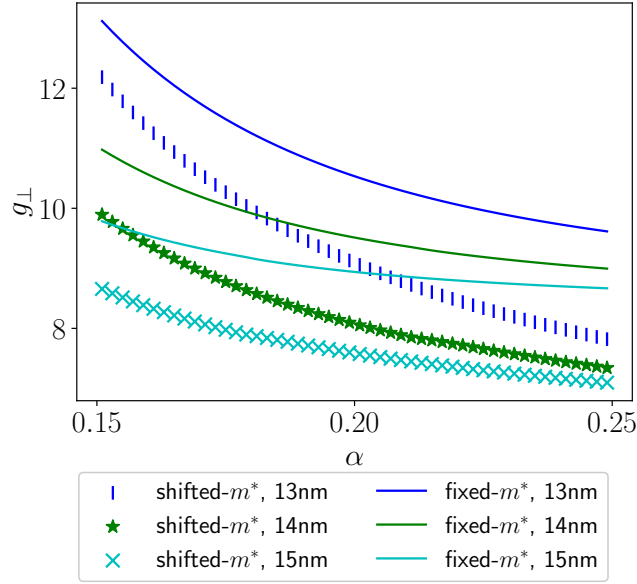


FIG. 13. Similar to Fig. 6 but with a different band alignment. The effective g_\perp has a stronger reduction in this paradigm.

[1] D. Loss and D. P. DiVincenzo, Phys. Rev. A **57**, 120 (1998).

[2] B. E. Kane, Nature **393**, 133 (1998).

[3] J. R. Petta, A. C. Johnson, J. M. Taylor, E. A. Laird, A. Yacoby, M. D. Lukin, C. M. Marcus, M. P. Hanson, and A. C. Gossard, Science **309**, 2180 (2005).

- [4] R. Hanson, L. P. Kouwenhoven, J. R. Petta, S. Tarucha, and L. M. K. Vandersypen, *Rev. Mod. Phys.* **79**, 1217 (2007).
- [5] R. Hanson and D. D. Awschalom, *Nature* **453**, 1043 (2008).
- [6] F. A. Zwanenburg, A. S. Dzurak, A. Morello, M. Y. Simmons, L. C. L. Hollenberg, G. Klimeck, S. Rogge, S. N. Coppersmith, and M. A. Eriksson, *Rev. Mod. Phys.* **85**, 961 (2013).
- [7] A. Chatterjee, P. Stevenson, S. De Franceschi, A. Morello, N. P. de Leon, and F. Kuemmeth, *Nature Reviews Physics* **3**, 157 (2021).
- [8] G. Scappucci, C. Kloeffel, F. A. Zwanenburg, D. Loss, M. Myronov, J.-J. Zhang, S. De Franceschi, G. Katsaros, and M. Veldhorst, *Nature Reviews Materials* **6**, 926 (2021).
- [9] Y. Fang, P. Philippopoulos, D. Culcer, W. A. Coish, and S. Chesi, *Materials for Quantum Technology* **3**, 012003 (2023).
- [10] É. I. Rashba, *Soviet Physics Uspekhi* **7**, 823 (1965).
- [11] J. Yoneda, K. Takeda, T. Otsuka, T. Nakajima, M. R. Delbecq, G. Allison, T. Honda, T. Kodera, S. Oda, Y. Hoshi, N. Usami, K. M. Itoh, and S. Tarucha, *Nature Nanotechnology* **13**, 102 (2018).
- [12] D. M. Zajac, A. J. Sigillito, M. Russ, F. Borjans, J. M. Taylor, G. Burkard, and J. R. Petta, *Science* **359**, 439 (2018).
- [13] A. Noiri, K. Takeda, T. Nakajima, T. Kobayashi, A. Sammak, G. Scappucci, and S. Tarucha, *Nature* **601**, 338 (2022).
- [14] A. R. Mills, C. R. Guinn, M. J. Gullans, A. J. Sigillito, M. M. Feldman, E. Nielsen, and J. R. Petta, *Science Advances* **8**, eabn5130 (2022).
- [15] X. Xue, M. Russ, N. Samkharadze, B. Undseth, A. Sammak, G. Scappucci, and L. M. K. Vandersypen, *Nature* **601**, 343 (2022).
- [16] G. Burkard, T. D. Ladd, A. Pan, J. M. Nichol, and J. R. Petta, *Reviews of Modern Physics* **95**, 025003 (2023), rMP.
- [17] L. M. Woods, T. L. Reinecke, and R. Kotlyar, *Phys. Rev. B* **69**, 125330 (2004).
- [18] D. V. Bulaev and D. Loss, *Phys. Rev. Lett.* **95**, 076805 (2005).
- [19] R. Danneau, O. Klochan, W. R. Clarke, L. H. Ho, A. P. Micolich, M. Y. Simmons, A. R. Hamilton, M. Pepper, D. A. Ritchie, and U. Zülicke, *Physical Review Letters* **97**, 026403 (2006), pRL.
- [20] D. M. Gvozdić and U. Ekenberg, *Physica Scripta* **2006**, 21 (2006).
- [21] D. V. Bulaev and D. Loss, *Phys. Rev. Lett.* **98**, 097202 (2007).
- [22] D. Heiss, S. Schaeck, H. Huebl, M. Bichler, G. Abstreiter, J. J. Finley, D. V. Bulaev, and D. Loss, *Phys. Rev. B* **76**, 241306 (2007).
- [23] D. Klauser, D. V. Bulaev, W. A. Coish, and D. Loss, Electron and hole spin dynamics and decoherence in quantum dots, in *Semiconductor Quantum Bits* (World Scientific, 2007) Chap. 10.
- [24] J. Fischer, W. A. Coish, D. V. Bulaev, and D. Loss, *Phys. Rev. B* **78**, 155329 (2008).
- [25] S. Roddaro, A. Fuhrer, P. Brusheim, C. Fasth, H. Q. Xu, L. Samuelson, J. Xiang, and C. M. Lieber, *Physical Review Letters* **101**, 186802 (2008), pRL.
- [26] C.-Y. Hsieh, R. Cheriton, M. Korkusinski, and P. Hawrylak, *Phys. Rev. B* **80**, 235320 (2009).
- [27] F. A. Zwanenburg, C. E. W. M. van Rijmenam, Y. Fang, C. M. Lieber, and L. P. Kouwenhoven, *Nano Letters* **9**, 1071 (2009), doi: 10.1021/nl803440s.
- [28] C. Kloeffel, M. Trif, P. Stano, and D. Loss, *Phys. Rev. B* **88**, 241405 (2013).
- [29] H. Watzinger, C. Kloeffel, L. Vukušić, M. D. Rossell, V. Sessi, J. Kukučka, R. Kirchschrager, E. Lausecker, A. Truhlar, M. Glaser, A. Rastelli, A. Fuhrer, D. Loss, and G. Katsaros, *Nano Letters* **16**, 6879 (2016), pMID: 27656760.
- [30] C. Kloeffel, M. J. Rančić, and D. Loss, *Phys. Rev. B* **97**, 235422 (2018).
- [31] J. C. Abadillo-Uriel, J. Salfi, X. Hu, S. Rogge, M. J. Calderón, and D. Culcer, *Applied Physics Letters* **113**, 012102 (2018).
- [32] P. Machnikowski, K. Gawarecki, and L. Cywiński, *Phys. Rev. B* **100**, 085305 (2019).
- [33] K. Wang, G. Xu, F. Gao, H. Liu, R.-L. Ma, X. Zhang, Z. Wang, G. Cao, T. Wang, J.-J. Zhang, D. Culcer, X. Hu, H.-W. Jiang, H.-O. Li, G.-C. Guo, and G.-P. Guo, *Nature Communications* **13**, 206 (2022).
- [34] J. Fischer and D. Loss, *Phys. Rev. Lett.* **105**, 266603 (2010).
- [35] P. Szumniak, S. Bednarek, B. Partoens, and F. M. Peeters, *Phys. Rev. Lett.* **109**, 107201 (2012).
- [36] T. Kobayashi, J. Salfi, C. Chua, J. van der Heijden, M. G. House, D. Culcer, W. D. Hutchison, B. C. Johnson, J. C. McCallum, H. Riemann, N. V. Abrosimov, P. Becker, H.-J. Pohl, M. Y. Simmons, and S. Rogge, *Nature Materials* **20**, 38 (2021).
- [37] N. W. Hendrickx, W. I. L. Lawrie, M. Russ, F. van Riggelen, S. L. de Snoo, R. N. Schouten, A. Sammak, G. Scappucci, and M. Veldhorst, *Nature* **591**, 580 (2021).
- [38] F. Borsoi, N. W. Hendrickx, V. John, M. Meyer, S. Motz, F. van Riggelen, A. Sammak, S. L. de Snoo, G. Scappucci, and M. Veldhorst, *Nature Nanotechnology* **19**, 21 (2024).
- [39] C. X. Yu, S. Zihlmann, J. C. Abadillo-Uriel, V. P. Michal, N. Rambal, H. Niebojewski, T. Bedecarrats, M. Vinet, É. Dumur, M. Filippone, B. Bertrand, S. De Franceschi, Y.-M. Niquet, and R. Maurand, *Nature Nanotechnology* **18**, 741 (2023).
- [40] X. Zhang, E. Morozova, M. Rimbach-Russ, D. Jirovec, T.-K. Hsiao, P. C. Fariña, C.-A. Wang, S. D. Oosterhout, A. Sammak, G. Scappucci, M. Veldhorst, and L. M. K. Vandersypen, *Nature Nanotechnology* 10.1038/s41565-024-01817-9 (2024).
- [41] C. Kloeffel, M. Trif, and D. Loss, *Phys. Rev. B* **84**, 195314 (2011).
- [42] L. A. Terrazos, E. Marcellina, Z. N. Wang, S. N. Coppersmith, M. Friesen, A. R. Hamilton, X. D. Hu, B. Koiller, A. L. Saraiva, D. Culcer, and R. B. Capaz, *Physical Review B* **103**, ARTN 125201 10.1103/PhysRevB.103.125201 (2021), rv9xo Times Cited:57 Cited References Count:59.
- [43] S. Bosco and D. Loss, *Phys. Rev. Appl.* **18**, 044038 (2022).
- [44] Z. Wang, E. Marcellina, A. R. Hamilton, J. H. Cullen, S. Rogge, J. Salfi, and D. Culcer, *npj Quantum Information* **7**, 54 (2021).
- [45] A. Sarkar, Z. Wang, M. Rendell, N. W. Hendrickx, M. Veldhorst, G. Scappucci, M. Khalifa, J. Salfi, A. Saraiva, A. S. Dzurak, A. R. Hamilton, and D. Culcer,

- Phys. Rev. B **108**, 245301 (2023).
- [46] Z. N. Wang, A. Sarkar, S. D. Liles, A. Saraiva, A. S. Dzurak, A. R. Hamilton, and D. Culcer, Physical Review B **109**, ARTN 07542710.1103/PhysRevB.109.075427 (2024), ne0i8 Times Cited:1 Cited References Count:242.
- [47] C.-A. Wang, H. E. Ercan, M. F. Gyure, G. Scappucci, M. Veldhorst, and M. Rimbach-Russ, npj Quantum Information **10**, 102 (2024).
- [48] J. M. Luttinger and W. Kohn, Phys. Rev. **97**, 869 (1955).
- [49] M. G. Burt, Semiconductor Science and Technology **2**, 460 (1987).
- [50] M. G. Burt, Semiconductor Science and Technology **3**, 739 (1988).
- [51] M. G. Burt, Semiconductor Science and Technology **3**, 1224 (1988).
- [52] M. G. Burt, Journal of Physics: Condensed Matter **4**, 6651 (1992).
- [53] B. A. Foreman, Phys. Rev. B **48**, 4964 (1993).
- [54] C. Galeriu, *kp Theory of Semiconductor Nanostructures*, Ph.D. thesis, Worcester Polytechnic Institute (2005).
- [55] G. Bastard, *Wave mechanics applied to semiconductor heterostructures* (1990).
- [56] M. Altarelli, Phys. Rev. B **28**, 842 (1983).
- [57] R. Eppenga, M. F. H. Schuurmans, and S. Colak, Phys. Rev. B **36**, 1554 (1987).
- [58] L. C. Andreani, A. Pasquarello, and F. Bassani, Phys. Rev. B **36**, 5887 (1987).
- [59] G. Bir and G. Pikus, *Symmetry and Strain-induced Effects in Semiconductors*, A Halsted Press book (Wiley, 1974).
- [60] M. Willatzen and L. C. L. Y. Voon, *The k p Method* (Springer Berlin Heidelberg, 2009).
- [61] D. J. BenDaniel and C. B. Duke, Phys. Rev. **152**, 683 (1966).
- [62] G. Bastard, Phys. Rev. B **24**, 5693 (1981).
- [63] U. Ekenberg and M. Altarelli, Phys. Rev. B **30**, 3569 (1984).
- [64] M. F. H. Schuurmans and G. W. 't Hooft, Phys. Rev. B **31**, 8041 (1985).
- [65] D. A. Broido and L. J. Sham, Phys. Rev. B **31**, 888 (1985).
- [66] R. Winkler, M. Merkler, T. Darnhofer, and U. Rössler, Phys. Rev. B **53**, 10858 (1996).
- [67] B. Venitucci, L. Bourdet, D. Pouzada, and Y.-M. Niquet, Phys. Rev. B **98**, 155319 (2018).
- [68] A. Sammak, D. Sabbagh, N. W. Hendrickx, M. Lodari, B. Paquelet Wuetz, A. Tosato, L. Yeoh, M. Bollani, M. Virgilio, M. A. Schubert, P. Zaumseil, G. Capellini, M. Veldhorst, and G. Scappucci, Advanced Functional Materials **29**, 1807613 (2019).
- [69] B. Martinez, J. C. Abadillo-Uriel, E. A. Rodríguez-Mena, and Y.-M. Niquet, Phys. Rev. B **106**, 235426 (2022).
- [70] J. C. Abadillo-Uriel, E. A. Rodríguez-Mena, B. Martinez, and Y.-M. Niquet, Phys. Rev. Lett. **131**, 097002 (2023).
- [71] P. YU and M. Cardona, *Fundamentals of Semiconductors: Physics and Materials Properties*, Graduate Texts in Physics (Springer Berlin Heidelberg, 2010).
- [72] J. P. Dismukes, L. Ekstrom, and R. J. Paff, The Journal of Physical Chemistry **68**, 3021 (1964).
- [73] S. Galdin, P. Dollfus, V. Aubry-Fortuna, P. Hesto, and H. J. Osten, Semiconductor Science and Technology **15**, 565 (2000).